

## Light-trapping in dye-sensitized solar cells

Cite this: DOI: 10.1039/c3ee40185e

Stephen Foster\* and Sajeev John

We demonstrate numerically that photonic crystal dye-sensitized solar cells (DSSCs) can provide at least a factor of one-third enhancement in solar light absorption and power conversion efficiency relative to their conventional counterparts. Our design consists of a lattice of modulated-diameter TiO<sub>2</sub> nanotubes filled with TiO<sub>2</sub> nanoparticles and interstitial regions filled with electrolyte. This provides not only light trapping and absorption enhancement, but offers improved electrical transport through the nanotube walls. The nanotube array itself forms an extended 2D photonic crystal, and the spacing and diameter of tubes in the array are chosen to promote dielectric modes that concentrate light in the interior of the tubes. Linear and sinusoidal modulation over select regions of the nanotube diameter create a 3D photonic crystal and allow for enhanced anti-reflection and back-reflection, respectively. Further reduction of reflection losses is accomplished through the addition of triangular corrugation to the glass–air interface of the cell. Using a constant volume of dye-coated TiO<sub>2</sub> nanoparticles our design gives a maximum achievable photocurrent density (MAPD) of 20.8 mA cm<sup>-2</sup> in 2D simulations. This is a 33% improvement over the MAPD for a simple planar cell geometry, and well above the record short-circuit current density for C101-based cells. We also demonstrate that choosing a dye with a broader but weaker absorption profile compared to commonly used dyes would lead to even larger absorption enhancements.

Received 18th January 2013

Accepted 7th March 2013

DOI: 10.1039/c3ee40185e

www.rsc.org/ees

## Broader context

The earth receives approximately  $1.7 \times 10^{17}$  W of power from the sun, exceeding current human energy consumption by many orders of magnitude. Harnessing this energy in a cost effective manner requires the use of more efficient and less expensive photovoltaics than those currently available. One promising technology being extensively researched is the dye-sensitized solar cell (DSSC). These cells are inexpensive to make and boast power conversion efficiencies of up to 12%. However in order to compete with other photovoltaics on the market, further efficiency gains are required. Photonic crystals offer one route to improving the light harvesting capabilities of DSSCs. Photonic crystals are sub-wavelength-scale periodic nanostructures that have the unique ability to guide and trap light. In this work we numerically investigate a new design for a DSSC with integrated photonic crystal consisting of modulated-diameter TiO<sub>2</sub> nanotubes. The design is shown to absorb substantially more light than conventional cells using an equivalent amount of dye-coated active material. Numerical results suggest the potential for efficiencies well beyond the current record for DSSCs.

## 1 Introduction

Dye-sensitized solar cells (DSSCs) are a promising alternative to conventional silicon-based solar cells due to their low cost and moderate efficiency. The standard design for a DSSC, pioneered by Michael Grätzel and O'Regan,<sup>1</sup> consists principally of a layer of TiO<sub>2</sub> nanoparticles, ~10 μm thick with particle sizes of ~20 nm, sintered together to form a nanoporous network. These are coated with a light-absorbing dye, typically a ruthenium complex. Photoexcited electrons are transferred from the dye to the conduction band of the TiO<sub>2</sub>, where they diffuse through the porous network to a transparent conducting oxide (TCO) substrate. A redox couple in solution (typically iodide–triiodide) fills the cell and transports electrons from cathode to

anode where they regenerate (reduce) dye molecules. Currently the highest efficiency achieved for a DSSC under standard AM 1.5 conditions<sup>2</sup> is 12.3%, reported by Grätzel *et al.* in 2011. This is a significant improvement over the previous record, which had remained constant at ~11% for several years.<sup>3–7</sup> As we show in this paper, significant further gains in efficiency are possible through photonic crystal based light trapping.<sup>8</sup>

There are three main obstacles preventing current DSSCs from attaining higher efficiencies: (i) significant losses of potential occur as electrons are transferred to dye molecules from the redox couple, resulting in a lower open circuit voltage ( $V_{OC}$ ), (ii) weak absorption in the near-infrared portion of the spectrum, limiting the short circuit current density ( $J_{SC}$ ), and (iii) recombination losses in the highly disordered nanoporous TiO<sub>2</sub> layer through which it is difficult for electrons to diffuse down to the TCO substrate. Much of the current research on DSSCs is focused on solving one of these three problems. In this

University of Toronto, Department of Physics, 60 St. George St., M5S 1A7, Toronto, Canada. E-mail: sfoster@physics.utoronto.ca; Fax: +1 416 978 7135; Tel: +1 416 978 5444

paper we address the issues of charge and light collection, but do not consider the chemistry problem of dye regeneration voltage losses.

A promising approach for improving charge collection is the replacement of the disordered nanoporous TiO<sub>2</sub> layer with a nanostructured photoelectrode. Zhang and Cao<sup>9</sup> and Yu *et al.*<sup>10</sup> review recent work on DSSCs using nanostructured photoelectrodes such as nanowires, nanotubes, nanoflowers, and branched nanowires, as well as methods for their preparation. The goal of these nanostructures is to improve charge collection by offering a direct pathway for electron transport, with reduced recombination.<sup>11</sup> Nanotube arrays have efficiencies in the range of 6–8%.<sup>12–16</sup> The primary factor limiting the efficiency of these devices is the lower surface area for dye absorption on the nanotube arrays compared to nanoporous TiO<sub>2</sub> layers. This tradeoff between superior light collection and charge collection has limited the use of previous nanostructures.

Attempts to circumvent this tradeoff involve composite cells, which utilize high surface area nanoparticles in combination with highly conductive nanotubes or nanowires. Various designs have been tried: nanoparticles deposited in a nanowire array,<sup>17,18</sup> nanoparticles coating the walls of nanotubes,<sup>19–21</sup> nanoparticles deposited in a nanotube array,<sup>22</sup> and nanotube arrays attached to nanoparticle layers.<sup>23,24</sup> These cells show significant improvement over nanostructured cells that have no added nanoparticles. However, none to date have approached the efficiencies of standard nanoparticle-based DSSCs. In this paper we demonstrate how a photonic crystal of nanotubes filled with nanoparticles can simultaneously enhance photonic and electronic management. Our proposed design is inspired by previous work on modulated nanowire Si solar cells,<sup>8</sup> where trapping light enabled structures with one micron equivalent bulk thickness of silicon to absorb nearly as much sunlight as a solid silicon slab more than 100 times as thick. These silicon nanostructures feature linear and sinusoidal modulation of the nanowire diameter for anti-reflection, light-trapping and back-reflection. The design makes use of the parallel interface refraction (PIR) effect,<sup>25</sup> in which incident light couples to modes propagating nearly parallel to the thin film–air interface. The effect provides longer dwell time for light in the active layer of the cell leading to substantially increased absorption.

In DSSCs, most research has focused on designing and testing new dyes. Few studies have considered improving light collection for a cell with a given dye. One method commonly employed in the most efficient DSSCs is to add a layer of larger (~400 nm) TiO<sub>2</sub> particles below the porous TiO<sub>2</sub> layer,<sup>2,4,6</sup> to increase the dwell time for light in the cell by diffuse random scattering.<sup>7</sup> Colodrero *et al.*<sup>26</sup> make use of alternating layers of porous SiO<sub>2</sub> and TiO<sub>2</sub> to create a 1D photonic crystal with stop-gap for back-reflection. Several groups have tried applying an inverse-opal photonic crystal mirror below the nanoporous TiO<sub>2</sub> layer.<sup>27–30</sup> Absorption enhancement arises here also due to slow photons within the photonic crystal itself.<sup>31</sup> However, applying a secondary photonic crystal separate from the active layer requires an extra manufacturing step, and good structural and electrical contact with the active layer is problematic.<sup>24</sup> Therefore it is advantageous to incorporate the photonic crystal

directly into the active layer. In nanotube-based cells this can be done by introducing a periodic modulation to the diameter of the nanotubes. The resulting 3D photonic crystal can be tuned to have a photonic stop-gap over a desired range of frequencies. Yip *et al.*<sup>24</sup> have used modulated nanotube arrays to achieve an efficiency of 7.11%.

Solar absorption is also improved by reducing reflection losses that occur at interfaces. Raut *et al.* review various anti-reflection strategies used in solar cells.<sup>32</sup> Although some DSSCs use a thin-film anti-reflective coating,<sup>33,34</sup> and others use internal nanostructures to reduce reflection,<sup>35,36</sup> there is little discussion of anti-reflection optimization.

Optical models of DSSCs have mostly assumed a simple Lambert–Beer exponential absorption in a planar active layer of the cell.<sup>37,38</sup> Some models include coherence effects and multiple reflections from interfaces,<sup>39</sup> and scattering from larger nanoparticles.<sup>40,41</sup> However, these one-dimensional models are inadequate for 2D and 3D photonic crystal DSSC's. A 2D finite-difference time-domain (FDTD) simulation of Maxwell's equations has been employed in one instance,<sup>42</sup> with the aim of optimizing geometrical parameters of dye-coated nanotubes.

In this paper a 2D formulation of the finite element method (FEM)<sup>43</sup> is used to solve Maxwell's equations in the frequency domain for arbitrary cell geometries. The fraction of incident light absorbed by the cell is computed for a range of frequencies and integrated over the AM 1.5 solar spectrum to give the maximum achievable photocurrent density (MAPD). Systematically varying geometrical parameters allows for optimization of the structure for high MAPD. Following previous work with silicon nanowires,<sup>8</sup> we propose and demonstrate the effectiveness of a new photonic crystal-based DSSC. The design consists of an array of large-diameter TiO<sub>2</sub> nanotubes filled with TiO<sub>2</sub> nanoparticles. Interstitial regions between nanotubes are filled with electrolyte, and the dielectric contrast between the interior and exterior of the nanotubes enables light-trapping. The array dimensions are optimized to focus trapped light in the interior of the nanotubes. Linear modulation of the nanotube diameter at the top of the array creates a graded index which reduces reflection at the TCO–TiO<sub>2</sub> interface. Sinusoidal modulation of diameter at the bottom of the array creates a 3D photonic crystal with a photonic stop-gap for back-reflection. The period of modulation is chirped linearly along each tube to give reflection over a broader range of frequencies. At off-normal incidence modulation further increases absorption due to the PIR effect. Triangular corrugation is added to the top of the cell at the air-glass interface to minimize reflection losses. The resulting cell absorbs substantially more light per unit volume of dye than a traditional DSSC, and has the potential for improved charge collection due to the connected conductive pathways of the nanotubes.

## 2 Theoretical model

We consider a 2D periodic nanostructure embedded in a thin-film dielectric stack, as depicted in Fig. 1. Incident light is treated as a plane wave with an arbitrary angle of incidence

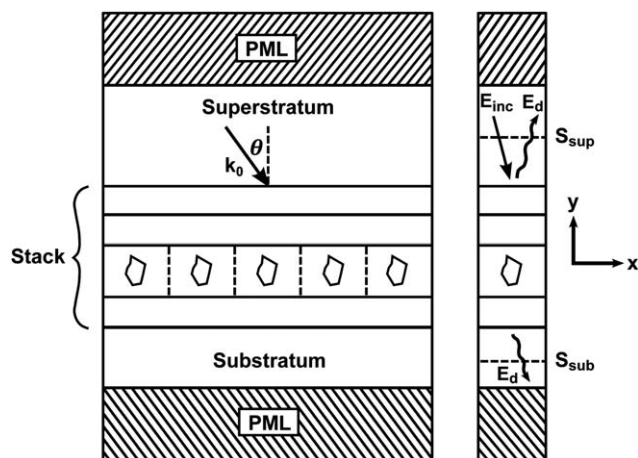


**Fig. 1** Diagram of the geometry studied in this work. We embed an arbitrarily shaped nanostructure in a thin film dielectric stack and solve for the case of a plane wave incident on the cell with a given angle. The geometry and dielectric function are periodic in the  $x$ -direction, so our computational domain contains only one nanostructure (shown on the right). Bloch boundary conditions are applied in the  $x$ -direction, and the domain is bounded above and below by perfectly matched layers (PMLs). For our calculations the magnetic field is polarized along the  $z$ -direction, out of the page.

$\theta$  and a wave vector  $\mathbf{k}_0 = k_0(\sin \theta \mathbf{x} - \cos \theta \mathbf{y})$ , where  $k_0 = \omega/c$ . Incident light is TE-polarized (magnetic field into the page) so that the electric field is polarized along the direction that the dielectric constant varies. This is representative of what incident light would encounter in a true three-dimensional array. The incident plane wave can be described by

$$\mathbf{E}_0 = A_0 \exp(i\mathbf{k}_0 \cdot \mathbf{r}), \quad (1)$$

where the amplitude is denoted  $A_0 = E_0(\cos \theta \mathbf{y} + \sin \theta \mathbf{x})$ , with  $E_0$  being an arbitrary complex number. We consider the solar spectrum to consist of an infinite incoherent superposition of such plane waves with wavelengths ranging from roughly 270 nm to 2.54  $\mu\text{m}$ .

In order to obtain the absorption for a given wavelength we solve Maxwell's equations for the electric and magnetic fields ( $\mathbf{E}$ ,  $\mathbf{H}$ ):

$$\nabla \times \mathbf{E} = i\omega\mu_0\mu\mathbf{H} \quad (2)$$

$$\nabla \times \mathbf{H} = -i\omega\epsilon_0\epsilon(\mathbf{r},\omega)\mathbf{E} \quad (3)$$

with a fixed frequency  $\omega$ , where  $\mu_0$  and  $\epsilon_0$  are the permeability and permittivity of free space. Relative permeability is denoted by  $\mu$  and is taken to be 1 for all materials considered. The complex-valued frequency-dependent dielectric function  $\epsilon(\mathbf{r},\omega)$  is spatially periodic in the  $x$ -direction. In the frequency domain, material dispersion is taken into account easily and accurately. Dielectric function data for all materials was obtained from Grätzel *et al.*,<sup>39</sup> with the exception of  $\text{TiO}_2$ , for which data was obtained from Rahman *et al.*<sup>44</sup> The dye-coated  $\text{TiO}_2$  nanoparticles and permeating electrolyte are treated as an effective medium with a single dielectric function. This is justified by the

sub-wavelength ( $\sim 20$  nm) feature sizes in this part of the medium.

Eqn (2) and (3) can be combined into a single equation

$$\nabla \times \left( \frac{1}{\epsilon(\mathbf{r},\omega)} \nabla \times \mathbf{H} \right) - k_0^2 \mu \mathbf{H} = 0, \quad (4)$$

which we solve for  $\mathbf{H}$ . The magnetic field is used because it is polarized entirely along the  $z$ -axis, allowing eqn (4) to be written as a scalar equation. The electric field  $\mathbf{E}$  can be recovered from  $\mathbf{H}$  using eqn (3). Eqn (4) is solved using an FEM formulation, described in detail in Demésy *et al.*<sup>43</sup>

Once  $\mathbf{E}$  and  $\mathbf{H}$  are known, quantities of interest such as absorption, reflection and transmission coefficients are calculated as follows. We define an incident field  $\mathbf{E}_{\text{inc}}$  that is equal to  $\mathbf{E}_0$  in the superstratum (air region) above the cell, and is zero in all other regions. From this the diffracted field is defined as  $\mathbf{E}_d \equiv \mathbf{E} - \mathbf{E}_{\text{inc}}$ . The diffracted field is the field that results from  $\mathbf{E}_{\text{inc}}$  impinging on the cell. The magnetic fields  $\mathbf{H}_{\text{inc}}$  and  $\mathbf{H}_d$  are defined in an analogous manner. Reflection and transmission coefficients can then be computed from the ratios:

$$r(\lambda, \theta) = \frac{\int_{S_{\text{sup}}} -\Re\{\mathbf{E}_d \times \mathbf{H}_d^*\} \cdot \mathbf{n} dx}{\int_{S_{\text{sup}}} \Re\{\mathbf{E}_0 \times \mathbf{H}_0^*\} \cdot \mathbf{n} dx} \quad (5)$$

$$t(\lambda, \theta) = \frac{\int_{S_{\text{sub}}} \Re\{\mathbf{E}_d \times \mathbf{H}_d^*\} \cdot \mathbf{n} dx}{\int_{S_{\text{sup}}} \Re\{\mathbf{E}_0 \times \mathbf{H}_0^*\} \cdot \mathbf{n} dx} \quad (6)$$

$S_{\text{sup}}$  and  $S_{\text{sub}}$  are lines that bound the dielectric stack above and below, as shown in Fig. 1. They have unit normal vectors  $\mathbf{n}$  pointing in the direction of decreasing  $y$ . Outgoing power in the superstrate and substrate is obtained by calculating the Poynting vector flux of the diffracted field through  $S_{\text{sup}}$  and  $S_{\text{sub}}$ , respectively. These quantities are normalized to the incident power, given by the Poynting vector flux of the *incident* field through  $S_{\text{sup}}$ . The two ratios yield  $r(\lambda, \theta)$  and  $t(\lambda, \theta)$ , the fractions of light reflected and transmitted by the cell. Since  $\mathbf{E}_0$  is simply a plane wave defined in eqn (1), the denominators in eqn (5) and (6) reduce to  $(\mathbf{E}_0^2 a \sqrt{\epsilon_0/\mu_0}) / (2\cos \theta)$ .

Normalized absorption  $\alpha(\lambda, \theta)$  can be inferred by subtracting  $r(\lambda, \theta)$  and  $t(\lambda, \theta)$  from unity.  $\alpha(\lambda, \theta)$  can also be computed independently from the ratio

$$\alpha(\lambda, \theta) = \frac{\int_A \omega \epsilon_0 \Im m(\epsilon) |\mathbf{E}|^2 dx dy}{\int_{S_{\text{sup}}} \Re\{\mathbf{E}_0 \times \mathbf{H}_0^*\} \cdot \mathbf{n} dx} \quad (7)$$

In the numerator the dielectric power loss density is integrated over the area  $A$  of the solar cell yielding the total absorbed power. As above this quantity is normalized to the incident Poynting vector flux to get the fraction of incident power

absorbed by the solar cell. An advantage of this method is that by integrating over different regions of the cell separately, we can distinguish between “useful” radiation absorbed by the dye and “lost” radiation absorbed by other materials (*e.g.* the electrolyte). We denote by  $\alpha^{\text{dye}}(\lambda, \theta)$  the fraction of incident power absorbed by dye molecules in the active region of the cell. Because  $\alpha(\lambda, \theta)$  is computed using the field within the solar cell, it is determined independently of  $r(\lambda, \theta)$  and  $t(\lambda, \theta)$ , which are computed from the field in the superstrate and substrate respectively. The sum of the three quantities is compared to unity as a self-consistency check.

The MAPD is obtained from  $\alpha^{\text{dye}}(\lambda, \theta)$  using

$$J_{\lambda_{\min}}^{\lambda_{\max}}(\theta) = \int_{\lambda_{\min}}^{\lambda_{\max}} \frac{e\lambda}{hc} I(\lambda) \alpha^{\text{dye}}(\lambda, \theta) d\lambda, \quad (8)$$

where  $e$  is the electron charge,  $h$  is planck's constant, and  $c$  is the speed of light in a vacuum.  $I(\lambda)$  is the AM 1.5 solar light intensity incident on the cell per unit area per unit wavelength, assumed to be a collimated beam with an angle of incidence  $\theta$ . The quantity  $I(\lambda)\alpha^{\text{dye}}(\lambda, \theta)$  is divided by the photon energy  $hc/\lambda$  to obtain the number of photons absorbed per second per unit area per unit wavelength. MAPD assumes perfect charge collection; *i.e.*, that one absorbed photon results in one electric charge contributing to current. It is obtained by multiplying by  $e$  and integrating over relevant wavelengths. The actual short circuit current density (involving carrier recombination losses) is less than the MAPD. The off-normal performance of DSSCs is particularly important since DSSCs typically do not utilize sun tracking devices and much of their input is off-normal.

### 3 Results and discussion

#### 3.1 Nanotubes with linear modulation

We benchmark our DSSC performance using the optical model published by Grätzel *et al.*<sup>39</sup> They used a ray-tracing algorithm to determine absorption, reflection and transmission coefficients as a function of wavelength for simple slab DSSCs. The Grätzel cell from top to bottom consists of: glass superstrate (3.88 mm thick); fluorine-doped tin oxide (FTO) transparent conducting oxide (690 nm thick); effective medium of dye-coated TiO<sub>2</sub> nanoparticles/iodide–triiodide electrolyte (varying thicknesses); pure electrolyte (16  $\mu\text{m}$  thick); second FTO layer (360 nm thick); and glass substrate (2.22 mm thick). Two different dye systems were studied, Z907<sup>45</sup> and C101.<sup>46</sup> For a DSSC with an 11.2  $\mu\text{m}$  thick nanoparticle layer sensitized with C101 dye, the Grätzel cell exhibits an MAPD of 15.9  $\text{mA cm}^{-2}$ . In our FEM formulation, this cell yields an MAPD of 15.6  $\text{mA cm}^{-2}$ . The minor discrepancy between the two values is attributed to small differences in dielectric function data. We use this system (11.2  $\mu\text{m}$  TiO<sub>2</sub> layer, C101 dye) as our reference point for optimization, since it represents a typical DSSC. Most DSSCs today make use of a diffuse scattering layer to increase light absorption, which is not modelled in this case. We return to this topic in the section on real world performance.

Our proposed cell design consists of a periodic array of TiO<sub>2</sub> nanotubes filled with dye-coated TiO<sub>2</sub> nanoparticles and a

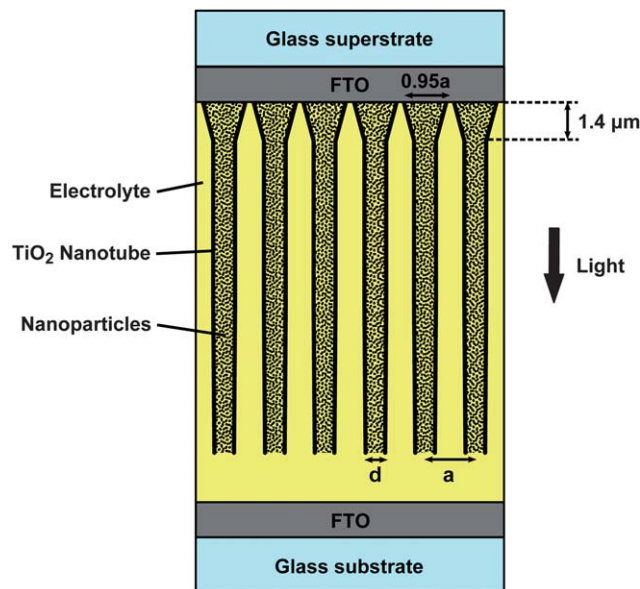


**Fig. 2** Proposed DSSC design (not to scale). An ordered TiO<sub>2</sub> nanotube array with period  $a$  and diameter  $d$  is attached to the upper FTO layer. The nanotube diameter is modulated linearly from  $d$  to  $0.95a$  over a  $1.4 \mu\text{m}$  region at the top of the array. The nanotubes are filled with TiO<sub>2</sub> nanoparticles, and permeating the entire cell is an iodide–triiodide electrolyte. Light is incident from the top.

permeating electrolyte, as shown in Fig. 2. Pure electrolyte fills the interstitial regions between nanotubes. We use Grätzel's FTO layer thicknesses of 690 nm and 360 nm. MAPD was found not to depend on the heights of the glass layers, so they were set to 1  $\mu\text{m}$  to reduce computational time. The thickness of the electrolyte layer between the nanotubes and the second FTO layer was also reduced to 1  $\mu\text{m}$ .

We optimize solar absorption at normal incidence for the simple geometry shown in Fig. 2 by varying the photonic crystal period  $a$  and tube diameter  $d$ . The nanotube diameter is linearly modulated over the top  $1.4 \mu\text{m}$  of the array to give a diameter of  $0.95a$  to better index match the FTO interface and reduce

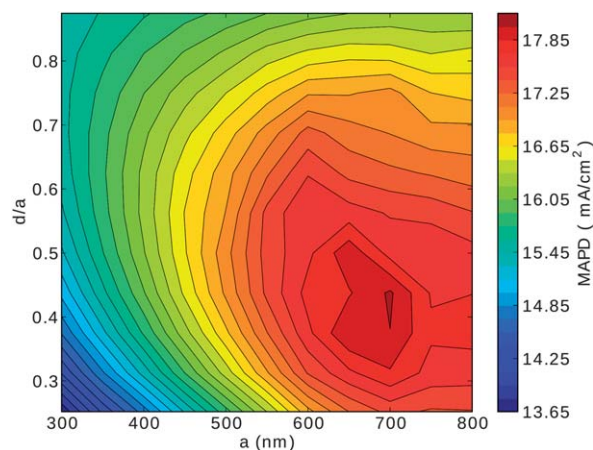


**Fig. 3** The MAPD  $J_{400\text{nm}}^{960\text{nm}}(0)$  in  $\text{mA cm}^{-2}$  for the nanotube array of Fig. 2 with normally incident light, as a function of the array periodicity  $a$  in nm and the nanotube diameter  $d$ . Equivalent slab thickness of TiO<sub>2</sub> nanoparticles is 11.2  $\mu\text{m}$  for all geometries considered. Nanotube wall thickness is set to  $0.1d$ . Optimal values are between roughly 650 nm and 720 nm for  $a$ , and  $0.35a$  and  $0.5a$  for  $d$ .

reflection. For all calculations in this paper the equivalent slab thickness of  $\text{TiO}_2$  nanoparticles is kept constant at  $11.2 \mu\text{m}$ . In other words, if the nanoparticles within the nanotubes were redistributed into a planar geometry, the layer would be  $11.2 \mu\text{m}$  thick. This ensures that absorption enhancement is due to light trapping rather than differences in the amount of active material. Equivalent slab thickness is maintained by adjusting the height of the nanotube array as parameters are varied. The nanotube wall thickness is set to  $0.1d$ .

Fig. 3b shows a map of  $J_{400\text{nm}}^{960\text{nm}}(0)$  (MAPD) as a function of  $a$  and  $d$ . The value of  $\lambda_{\text{min}}$  was set to  $400 \text{ nm}$  to match the value used by Grätzel *et al.*  $\lambda_{\text{max}}$  was set to  $960 \text{ nm}$ , above which dye absorption is effectively zero. The spectral range  $[400 \text{ nm}, 960 \text{ nm}]$  was spanned with step sizes of  $2 \text{ nm}$ . The data show a clear maximum in MAPD with a peak value of  $18.0 \text{ mA cm}^{-2}$ , an improvement of  $15.4\%$  over the planar Grätzel cell. The centre of the broad maximum in Fig. 3b occurs at  $(a, d) = (690 \text{ nm}, 0.42a)$ . The height of the nanotube array for these values is  $32.2 \mu\text{m}$ . We use these parameter values as a starting point in subsequent optimization with modulated nanotubes. The MAPD is enhanced over a wide range of values for  $a$  and  $d$ , indicating that the design is tolerant to fabrication errors.

Dye absorption spectra for the planar geometry and the best performing nanotube array geometry are compared in Fig. 4a. The nanotube array significantly outperforms the planar cell over a broad spectral range for  $\lambda > 600 \text{ nm}$ . At shorter wavelengths the array shows a slight decrease in dye absorption relative to the planar case, due to absorption by the additional electrolyte present between the nanotubes. The enhancement at longer wavelengths is caused primarily by dielectric modes of light that confine the electric field to the interior of the nanotubes. Fig. 4b shows a map of the electric field intensity  $|E|^2$  in the top half of the solar cell for an incident wavelength of  $700 \text{ nm}$ . The field intensity inside the nanotubes is enhanced by a factor of  $6.65$  relative to the incident plane wave.

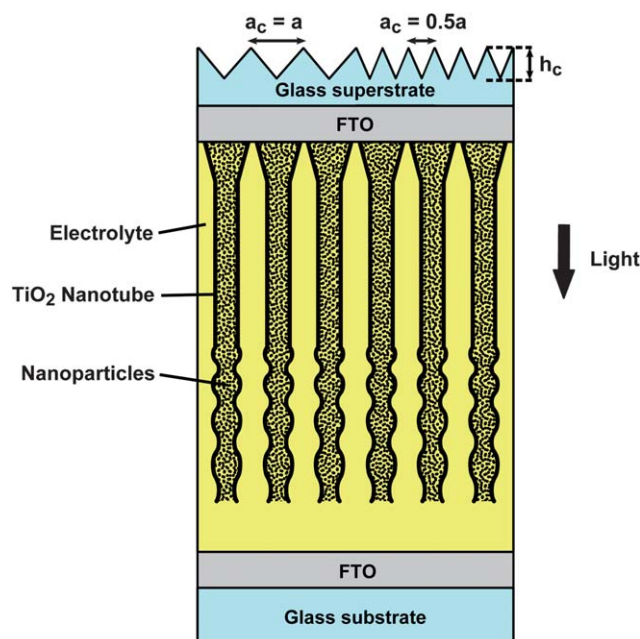


**Fig. 5** Cell geometry (not to scale) with linearly chirped sinusoidal modulation added to the lower portion of the nanotube array and triangular corrugation added to the air–glass interface. The modulation period increases towards the bottom of the array, with a constant amplitude  $A$ . The height of the modulated region is set to  $0.52$  times the total array height. The corrugation has height  $h_c$  and period  $a_c$ . We study the cases  $a_c = a$  (shown on the left of the diagram) and  $a_c = a/2$  (shown on the right).

### 3.2 Back-reflection with chirped photonic crystal mirror

DSSCs typically use a transparent conducting oxide as a back contact material, resulting in considerable optical transmission through the cell. Substantial performance improvements are possible by incorporating a back-reflector in the form of periodic modulation of the nanotube diameter to the bottom half of

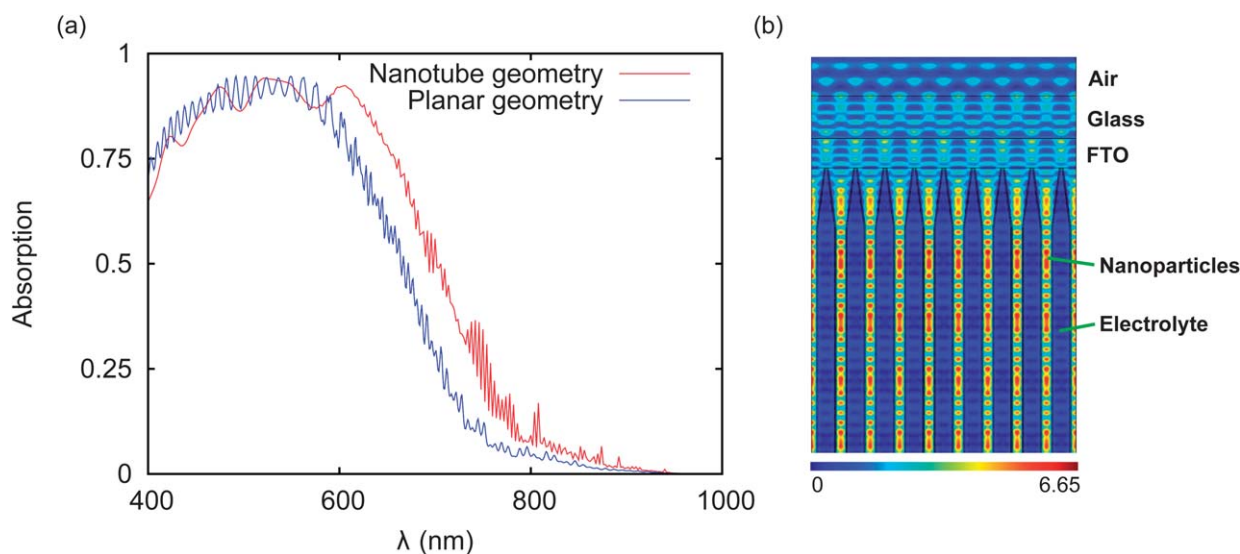


**Fig. 4** (a) Absorption spectra for the planar reference case (in blue) and the linearly modulated nanotube array with  $(a, d) = (690 \text{ nm}, 0.42a)$  (in red). A broad increase in absorption for the nanotube array over the planar case is seen in the wavelength range  $600\text{--}800 \text{ nm}$ . (b) For the nanotube array of (a), a spatial map of the electric field intensity  $|E|^2$  in the top half of the cell for  $\lambda = 700 \text{ nm}$ . Strong confinement of the field to the inside of the nanotubes is observed.

the array (see Fig. 5 – in this case there is no triangular corrugation at the top of the cell, so  $h_c = 0$ ). This forms the array into a 3D photonic crystal (modelled as 2D in this work). By adjusting the period and amplitude of the modulation and the dimensions of the array we create a 1D photonic stop gap in the  $y$ -direction. Adding a linear chirp to the modulation period broadens the stop gap to reflect an even wider range of wavelengths.

We apply to the nanotube radius  $r$  a modulation of the form  $r(y) = r_0 + A\cos(2\pi y/a_y)$ , where  $A$  is the modulation amplitude,  $a_y$  is the  $y$ -dependent modulation period, and  $r_0 = d/2$ . The period  $a_y$  is varied linearly along the length of the modulated region according to the formula  $a_y = a_1 + (a_2 - a_1)(y - y_0)/h$ , with  $h$  being the height of the modulated region. Using this formula gives a range of periods that is much greater than  $[a_1, a_2]$ . The observed range of periods is what we report in this paper when specifying the chirp, rather than  $a_1$  and  $a_2$ . We find an optimal  $h$  to be 0.52 times the total height of the array. MAPD depends strongly on the amplitude of modulation. The best performance was found for  $A = 80$  nm, the strongest modulation studied. Nevertheless we use  $A = 50$  nm in subsequent calculations since this may be more amenable to fabrication.

To optimize parameters an iterative approach was taken. Starting with  $a$  and  $d$  held fixed at 690 nm and  $0.42a$ , respectively, an optimal range was found for  $a_y$ . Next using this range for  $a_y$  and holding it fixed, new values for  $a$  and  $d$  were found. The process was repeated until the parameter values converged. Maximum solar absorption was found when  $(a, d) = (470$  nm,  $0.5a)$ , with a range of [230 nm, 425 nm] for  $a_y$  and a nanotube array height of  $27.2$   $\mu\text{m}$ . This provides MAPD of  $19.2$   $\text{mA cm}^{-2}$ , a 21.2% improvement over the planar geometry. The dye absorption spectrum for the modulated geometry (Fig. 6a) shows significant enhancement compared to other structures over a wide spectral range up to  $\lambda = 770$  nm. At longer wavelengths the modulation has almost no effect, suggestive of a 1D photonic stop-gap with a lower band edge at 770 nm. This stop-gap was verified by setting the imaginary part of the dye

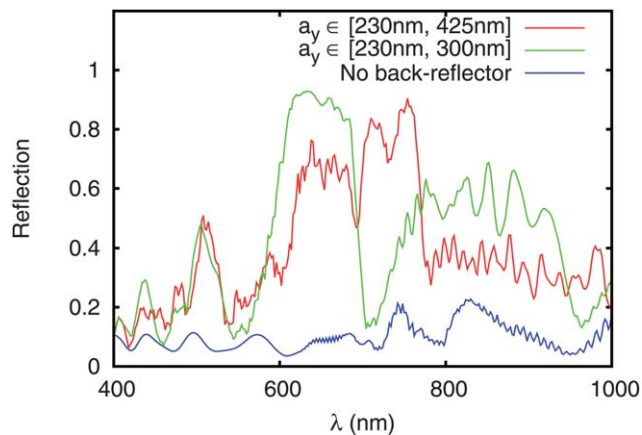


**Fig. 7** Reflection spectra with dye absorption turned off, for the optimized nanotube array of Fig. 6 (in red) and the planar geometry (in blue). Also shown in green is the reflection spectrum for the same nanotube array with a weaker chirp ( $a_y$  in the range [230 nm, 300 nm]). The weaker chirp gives a narrower but more highly reflecting stop-gap.

refractive index to zero and calculating the reflection spectrum (see Fig. 7). The optimized geometry with modulation has a clear reflection stop-gap extending from 620 to 770 nm with an average reflectivity of roughly 0.7. The lower edge of the gap at 770 nm corresponds precisely to the absorption enhancement cutoff in Fig. 6a. No stop-gaps are seen for unmodulated nanotubes.

Optimizing the chirp of the 1-D Bragg grating involves a tradeoff between the spectral width and quality of the stop-gap. A stronger chirp (*i.e.*, wider range in  $a_y$ ) tends to give a wider stop-gap but a lower overall reflectivity. If the period changes too quickly in space, the reflectivity is degraded at any given wavelength. This is seen in Fig. 7, where we also plot reflectivity for a weaker chirp with a range of [230 nm, 300 nm] for  $a_y$ . The more weakly chirped geometry has a narrower but stronger reflecting (85%) stop-gap, ranging from 600 to 700 nm.

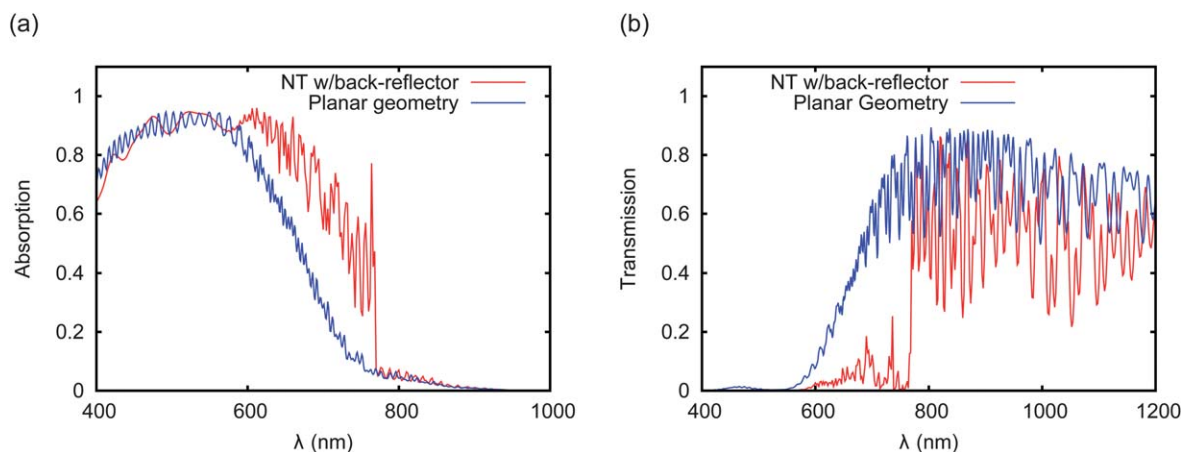


**Fig. 6** (a) Dye absorption spectra for nanotubes with chirped sinusoidal modulation (in red) and for the planar geometry (in blue). Optimal parameters for the new structure are  $(a, d) = (470$  nm,  $0.5a)$  with a range of [230 nm, 425 nm] for  $a_y$ . (b) Transmission spectra for the two cell geometries in (a). For wavelengths shorter than the stop-gap edge at 770 nm, transmission for our optimized geometry is strongly suppressed relative to the planar case.

An attractive feature of the photonic crystal mirror is frequency selectivity of absorption. This enables longer wavelength light to pass through the DSSC and potentially be harvested by a second solar cell below. Fig. 6b compares the transmission spectra for our optimized structure and the planar geometry. We characterize transmission in units of MAPD by defining:

$$T_{\lambda_{\min}}^{\lambda_{\max}}(\theta) = \int_{\lambda_{\min}}^{\lambda_{\max}} \frac{e\lambda}{hc} I(\lambda) t(\lambda, \theta) d\lambda \quad (9)$$

$T_{\lambda_{\min}}^{\lambda_{\max}}(\theta)$  is a measure of the short circuit current density that would result if all transmitted photons in the range  $[\lambda_{\min}, \lambda_{\max}]$  were collected by a secondary solar cell and converted to current with 100% efficiency. We use the wavelength range [800 nm, 1200 nm] for evaluating performance in regards to transmission. While a significant amount of light in this range is transmitted, our optimized design yields a transmitted MAPD of  $10.2 \text{ mA cm}^{-2}$  compared to  $13.9 \text{ mA cm}^{-2}$  for the planar solar cell.

### 3.3 Corrugation of glass-air interface

Typical reflection losses in our simulations are about 10% of incident power for a cell with no back-reflector (*cf.* Fig. 6b). To reduce reflection we introduce a triangular corrugation at the glass-air interface, as shown in Fig. 5. The nature of our computational method limits the corrugation period  $a_c$  to integer fractions of the nanotube array period ( $a$ ,  $a/2$ ,  $a/3$ , etc.). The cases  $a_c = a$  and  $a_c = a/2$  were chosen for study as these numbers fall into the range of previously reported optimal periods for nanostructured anti-reflective arrays.<sup>47</sup> For calculations involving corrugation, the height of the glass layer was increased to  $10 \mu\text{m}$  to be realistic. Absorption was found to vary significantly as the corrugation was shifted horizontally relative to the nanotube array due to local wave interference. To simulate solar illumination we average over several different

positions of the corrugation relative to the nanotube array. Starting with the optimized structure of Section 3.2 we investigate the dependence of cell performance on the corrugation height  $h_c$ .

MAPD as a function of corrugation height is shown in Fig. 8 for  $(a, d) = (470 \text{ nm}, 0.5a)$  with  $a_y$  in the range [230 nm, 425 nm], for corrugation periods  $a_c = 235 \text{ nm}$  and  $a_c = 470 \text{ nm}$ . For both corrugation periods MAPD increases with  $h_c$  up to  $h_c \approx 200 \text{ nm}$ , after which it plateaus. At all heights the cell with  $a_c = 235 \text{ nm}$  outperforms the cell with  $a_c = 470 \text{ nm}$ . MAPD reaches a high of  $20.6 \text{ mA cm}^{-2}$  for the former, and only  $20.1 \text{ mA cm}^{-2}$  for the latter. In both cases the improvement over cells with no corrugation is substantial, indicating a sizable reduction of reflection losses. Since much of the reflection arises from the stop-gap, we rerun the simulation without any sinusoidal modulation of the nanotube diameter. Fig. 9 shows the reflection spectra under this setup for the corrugation period  $a_c = a/2$  with  $h_c = 600 \text{ nm}$ . Also shown for reference is the reflection spectrum with  $h_c$  set to zero (*i.e.*, no corrugation). Reflection is dramatically lower in the corrugated case: roughly 1% of all light is reflected for wavelengths up to  $\lambda = 700 \text{ nm}$ . Above this we see two peaks where reflection rises to about 15%. However even at these peaks the reflection coefficient is below that of the uncorrugated case. Total reflection losses over the range [400 nm, 960 nm] as a fraction of the incident power are 4.1% for the corrugated cell, compared to 9.9% with no corrugation.

To obtain a final optimized structure the cell parameters ( $a$ ,  $d$ , and the range of  $a_y$ ) are re-optimized with corrugation in place using  $a_c = a/2$  and  $h_c = 600 \text{ nm}$ . The same iterative optimization procedure described in Section 3.2 is used. After optimization the new values for the cell parameters are  $a = 490 \text{ nm}$  and  $d = 0.48a$ , with a range for  $a_y$  of [240 nm, 425 nm]. The height of the nanotube array for these parameters is  $28.3 \mu\text{m}$ . In Fig. 10 we compare the absorption spectrum for the new structure with the planar geometry. The optimized structure outperforms the planar cell by a significant margin and is

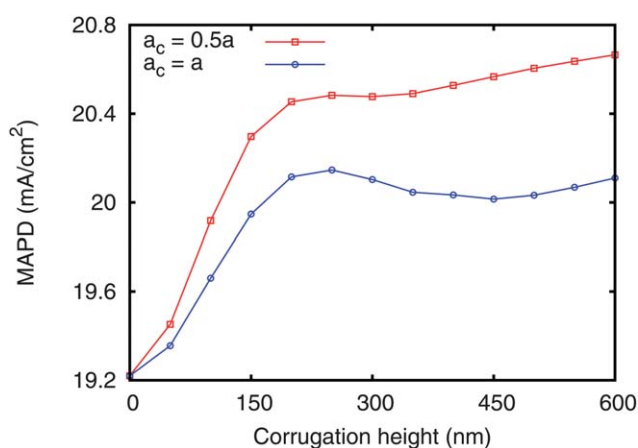


**Fig. 8** MAPD as a function of the corrugation height  $h_c$  for the corrugation periods  $a_c = a$  (red line) and  $a_c = a/2$  (blue line). The cell parameters are  $(a, d) = (470 \text{ nm}, 0.5a)$  with  $a_y$  in the range [230 nm, 425 nm]. The smaller corrugation period  $a_c = a/2$  yields better performance at all corrugation heights.

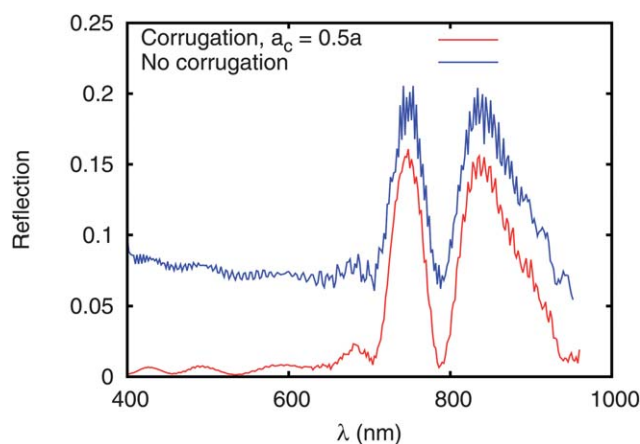


**Fig. 9** Comparison of the reflection spectra for the nanotube geometry with corrugation ( $a_c = a/2$  and  $h_c = 600 \text{ nm}$ ) (in red) and without corrugation (in blue). For both cells the chirped modulation has been turned off to eliminate back-reflection from the photonic crystal. Nanotube parameters for both cases are  $(a, d) = (470 \text{ nm}, 0.5a)$ .

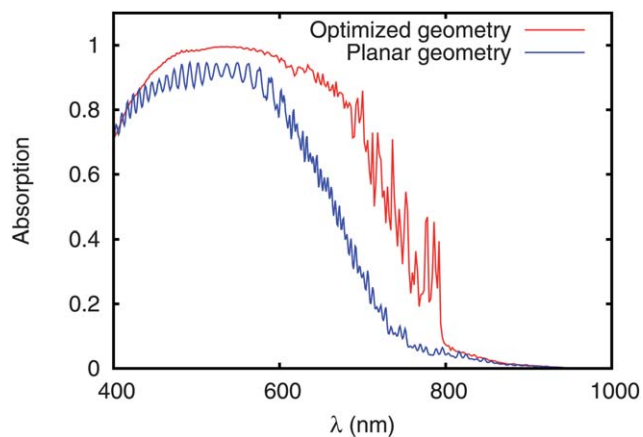


**Fig. 10** Comparison of the dye absorption spectra for the final optimized structure with corrugation of the glass–air interface (red line), and the reference planar geometry (blue line). The optimized nanotube design outperforms the planar geometry by a substantial margin at all wavelengths. Due to the addition of a strong anti-reflection layer, there is a broad spectral region from roughly 480 to 600 nm over which essentially all light is absorbed.

**Table 1** Summary of results obtained for the different geometries studied. The first column shows MAPD and the second shows percent improvement over the planar geometry MAPD. Additions to the cell structure are cumulative; each geometry listed also has the features of the previous

Geometry	MAPD ( $\text{mA cm}^{-2}$ )	% Improvement
Planar	15.6	—
Linearly modulated NT	18.0	15.4
Sinusoidal modulated NT	19.2	21.2
Glass corrugation NT	20.8	33.5

more absorbing at all wavelengths. In the spectral region from 480 to 600 nm the absorption coefficient is essentially unity. The stop-gap edge is shifted from 770 nm to 800 nm for the new geometry. The MAPD for the new structure is  $20.8 \text{ mA cm}^{-2}$ , an improvement of 33.5% relative to the planar case.

Table 1 summarizes our results, listing MAPD and the percentage improvement over the planar case for each geometry considered.

### 3.4 Real world performance

Thus far we have compared our design with a simple planar geometry DSSC. However our design also outperforms the state-of-the-art highest efficiency DSSCs, which use a layer of large diameter  $\text{TiO}_2$  nanoparticles to provide random back-scattering of light. The record for short-circuit current density in such a C101-based DSSC is  $17.94 \text{ mA cm}^{-2}$ , by Gao *et al.*<sup>46</sup> Our MAPD value surpasses this number and yields a significantly improved short-circuit current density, even if we assume a typical recombination loss of  $1.5 \text{ mA cm}^{-2}$ .<sup>39</sup> Short-circuit current densities comparable to our MAPD have been reported,<sup>7</sup> but such cells use different dyes and therefore can't be directly compared with ours. Photonic crystal light trapping clearly offers advantages over random light scattering used in most cells.

As pointed out by Gálvez *et al.*,<sup>48</sup> the best light-trapping design for a given cell may not yield the highest efficiency, depending on the charge generation profile and charge transport properties. A full electrical simulation of our cell is beyond the scope of this paper, but values in the literature can act as a rough guide. Typical electron diffusion lengths in  $\text{TiO}_2$  nanoparticle layers are  $\sim 20$  to  $30 \mu\text{m}$ ,<sup>39</sup> compared with up to  $100 \mu\text{m}$  for  $\text{TiO}_2$  nanotubes.<sup>49</sup> Adding nanoparticles to a nanotube electrode has been found to reduce the electron diffusion length by  $\sim 15$  to 25% from the bare nanotube value.<sup>20,22</sup> For the best nanotube arrays this would give a diffusion length of  $75 \mu\text{m}$  or more, much greater than the nanotube length in our design. Moreover, our photonic crystal mirror tends to confine charge generation to the upper half of the nanotube array, closer to the electrode. Charge collection efficiencies for our design should therefore be very high. For materials with a lower diffusion length, our design would still be effective, but a shortened nanotube array would be required to compensate for the reduced charge collection. Ultimately the optimal height of the nanotube array in any real cell will be determined by the tradeoff that exists between light harvesting and charge collection.

For the purposes of estimating power conversion efficiency we assume that a negligible fraction of generated electrons are lost and that our MAPD of  $20.8 \text{ mA cm}^{-2}$  translates into the actual short circuit current density. We use Gao's 11% efficient cell as a reference, and assume the other cell parameters (open circuit voltage, fill factor) remain unchanged. This gives a lower bound on power conversion efficiency of 12.75%, with further improvement likely from higher open-circuit voltage (due to reduced recombination) not included in our estimate. An even higher short-circuit current density is possible if charge collection efficiencies are high enough to permit a longer nanotube array.

### 3.5 Angular performance

An important consideration in solar cell performance is absorption at off-normal angles of incidence. DSSCs are often either pointed in a fixed direction or attached to a portable device so that a significant fraction of sunlight impinges from an off-normal angle. Fig. 11 compares MAPD as a function of the incident angle  $\theta$  for the optimized structure of Section 3.3 and the planar cell. For each angle  $\theta$  it is assumed that the entire AM 1.5 spectrum is collimated and incident on the cell at angle  $\theta$  with TE polarization. Our optimized structure displays very good performance at low angles, with MAPD well above that of the planar case. However at higher angles the MAPD decreases, and the optimized design actually performs slightly worse than the planar geometry for angles above  $50^\circ$ . Our design nevertheless outperforms the planar geometry when averaging over all angles.

We also consider a structure that performs uniformly well at all angles of incidence by optimizing geometrical parameters for performance at  $0^\circ$ ,  $35^\circ$ , and  $70^\circ$  with equal weight. Optimal cell parameters under these constraints were found to be  $(a, d) = (620 \text{ nm}, 0.75a)$  with a range of  $[235 \text{ nm}, 415 \text{ nm}]$  for  $a_y$ .

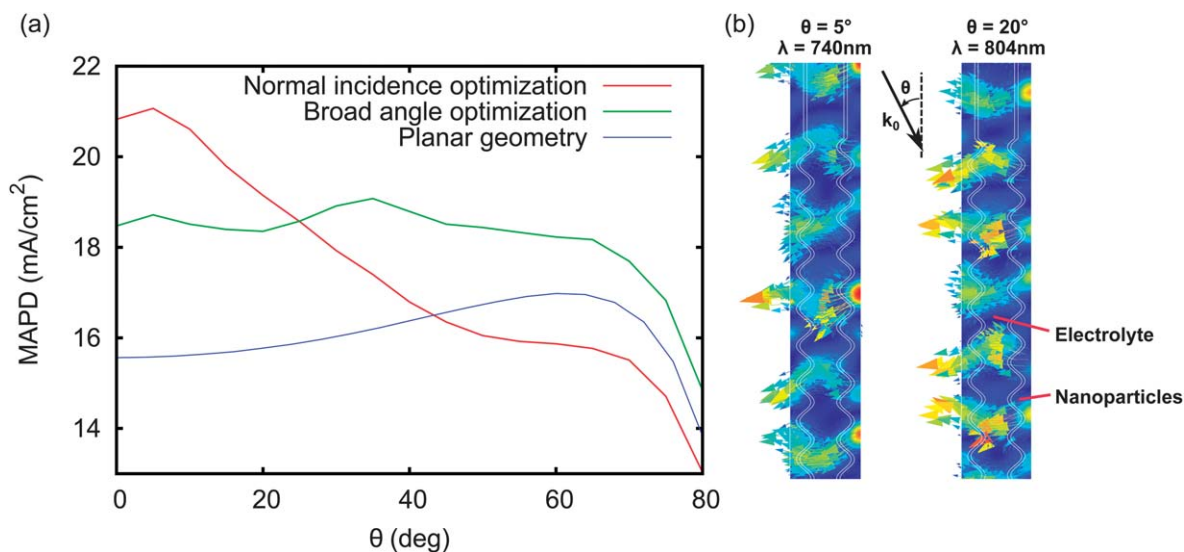


**Fig. 11** (a) MAPD as a function of the angle of incidence  $\theta$  for several cell geometries. The red curve shows MAPD for our final optimized nanotube array with  $(a, d) = (490 \text{ nm}, 0.48a)$  and a range of  $[230 \text{ nm}, 425 \text{ nm}]$  for  $a_y$ . The green curve shows MAPD for a nanotube array with geometry optimized for broad-angle acceptance:  $(a, d) = (620 \text{ nm}, 0.75a)$  and a range of  $[235 \text{ nm}, 415 \text{ nm}]$  for  $a_y$ . MAPD for the planar geometry is shown in blue. (b) Time-averaged Poynting vector and field intensity maps inside the cell for the normal incidence-optimized geometry. The two cases shown are  $\theta = 5^\circ$ ,  $\lambda = 740 \text{ nm}$  (left), and  $\theta = 20^\circ$ ,  $\lambda = 804 \text{ nm}$  (right). Light is incident from the top-left. Both cases show a clear PIR effect: the Poynting vector is pointed left (negative refraction) and is nearly parallel to the air-glass interface.

The MAPD for the new optimized geometry is  $18.5 \text{ mA cm}^{-2}$  at normal incidence, and remains roughly constant with angle up to  $\theta = 70^\circ$ , as shown in Fig. 11. The new structure is outperformed by the previous optimized geometry at low angles of incidence, but has a much higher MAPD when averaged over all angles.

At off-normal angles of incidence, absorption is enhanced through parallel interface refraction (PIR), an anomalous type of negative refraction seen in certain photonic crystal architectures. Light undergoing PIR couples to modes nearly parallel to the surface of the photonic crystal, yielding long dwell times in the active layer of the cell. Fig. 11b shows the time-averaged Poynting vector and electric field intensity  $|E|^2$  inside the nanotube array for the normal incidence-optimized geometry, for two different incident waves ( $\theta = 5^\circ$ ,  $\lambda = 740 \text{ nm}$ , and  $\theta = 20^\circ$ ,  $\lambda = 804 \text{ nm}$ ). These incident waves correspond to peaks in the absorption spectrum. In both cases we see a strong PIR effect, with Poynting vectors oriented in the negative  $x$ -direction and nearly parallel to the cell surface. PIR was observed over a wide range of angles and wavelengths, in particular for the broad acceptance angle geometry.

### 3.6 Alternative dye systems

Although we have focused on the C101 dye in this work, our light-trapping strategy is even more effective in dyes with a long absorption tail and a broad spectral range with low but non-negligible absorption. In contrast, a dye with an absorption profile that falls off quickly with wavelength exhibits relatively less light-trapping enhancement.

We illustrate this with a simple model. A pair of Lorentzian curves are fit to the imaginary part of the refractive index for the C101 effective medium. The original data and the fit are shown

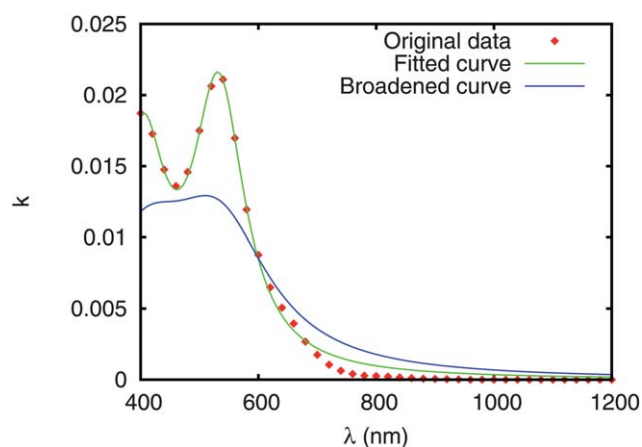


**Fig. 12** Red diamonds: data used in this paper for the imaginary component of the refractive index for the C101-based effective medium. Shown in blue is a fit of two Lorentzian peaks to this data. The green line is obtained by doubling the scale parameter of the two Lorentzian peaks to create a broader curve for study.

in Fig. 12. The fit overestimates the data for higher wavelengths, but provides a plausible absorption spectrum with a mathematical form that can be manipulated. The fitted curve is broadened by doubling the scale parameter for each of the Lorentzian curves (while leaving the amplitude and central wavelength unchanged). This gives a second absorption spectrum with a lower peak but a much longer absorption tail, also shown in Fig. 12. We optimize the cell structure for this broadened spectrum and determine the enhancement in MAPD relative to the planar case. This is compared with the 33.5% improvement in MAPD obtained for the original dye spectrum. For these calculations the real part of the refractive index is left unchanged from the original C101 effective medium.

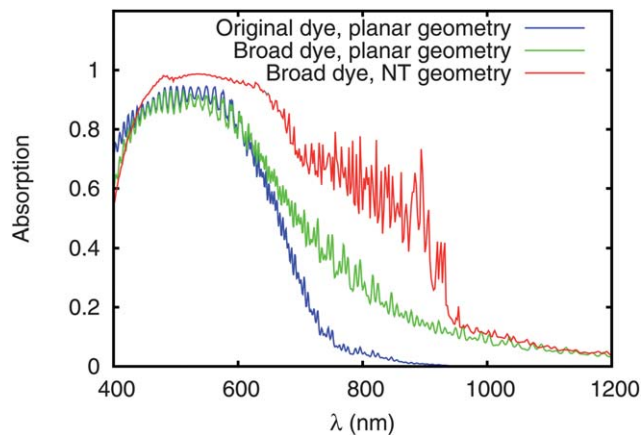


**Fig. 13** Absorption coefficient for three different dye–geometry systems: unaltered C101 dye with a planar geometry (red curve), broadened dye with planar geometry (green curve), and broadened dye with optimized nanotube geometry (blue curve). Structural parameters for the optimized geometry are  $(a, d) = (600 \text{ nm}, 0.47a)$  with a range for  $a_y$  of  $[265 \text{ nm}, 440 \text{ nm}]$ . Absorption enhancement over the planar cell occurs for a wider range of wavelengths than in the case of the original dye.

For reference we calculate absorption in the planar case, again assuming an  $11.2 \mu\text{m}$  thick layer of the effective medium. Because our broadened dye absorbs at much longer wavelengths than the original dye, we extend our calculation range to  $[400 \text{ nm}, 1200 \text{ nm}]$ . The absorption coefficient for the original dye and broadened dye with planar geometry are shown in Fig. 13. The new broad spectrum dye has significantly higher absorption overall. The decrease in peak absorption due to broadening is much less significant than the increase in absorption at higher wavelengths. The MAPD for the new dye in a planar cell is  $19.74 \text{ mA cm}^{-2}$ .

In optimizing the cell structure for the broadened dye we vary  $a$ ,  $d$ , and the range of  $a_y$ ; all other geometrical parameters

are unchanged from previous sections. The same iterative approach for optimization described in Section 3.2 is used. After completing this procedure we arrive at parameter values of  $(a, d) = (600 \text{ nm}, 0.47a)$  with a range for  $a_y$  of  $[265 \text{ nm}, 440 \text{ nm}]$ . As expected a large increase in absorption relative to the planar case is seen for the optimized cell (Fig. 13). A photonic stop-gap edge is observed around  $950 \text{ nm}$ . The most notable difference from the original optimized design is the length scale of the relevant parameters. The nanotube array has a much larger period than before, and the chirped modulation has both a larger average period and a wider range of periods. This has the effect of shifting the absorption enhancement to longer wavelengths and over a wider range. The MAPD for the new parameters is  $27.2 \text{ mA cm}^{-2}$ , a 37.8% improvement over the planar cell. Clearly, our design provides the most performance enhancement for dyes with a broad absorption spectrum, even if peak absorption is relatively low. This ties in well with current research being done on panchromatic absorption in DSSCs.<sup>50</sup>

### 3.7 Fabrication strategy

In this section we discuss how our proposed design could be made with current manufacturing techniques. Many different methods for preparing  $\text{TiO}_2$  nanotubes have been developed, including sol–gel techniques,<sup>51</sup> coating of ZnO nanowires,<sup>52,53</sup> direct anodization of Ti foil,<sup>13–15</sup> and deposition of a  $\text{TiO}_2$  layer into an anodized alumina template.<sup>54,55</sup> The latter two techniques, based on anodization, enable formation of highly ordered nanotube arrays. Direct Ti foil anodization is widely used in DSSC research, and is capable of producing nanotubes with a wide range of geometrical parameters. These nanotubes can have heights of up to hundreds of microns,<sup>14</sup> diameters of up to  $350 \text{ nm}$ , and tube-to-tube spacings of up to  $500 \text{ nm}$ .<sup>19,56</sup> The main drawback of the direct anodization method is lack of selectivity. To construct a cell with our design we need to

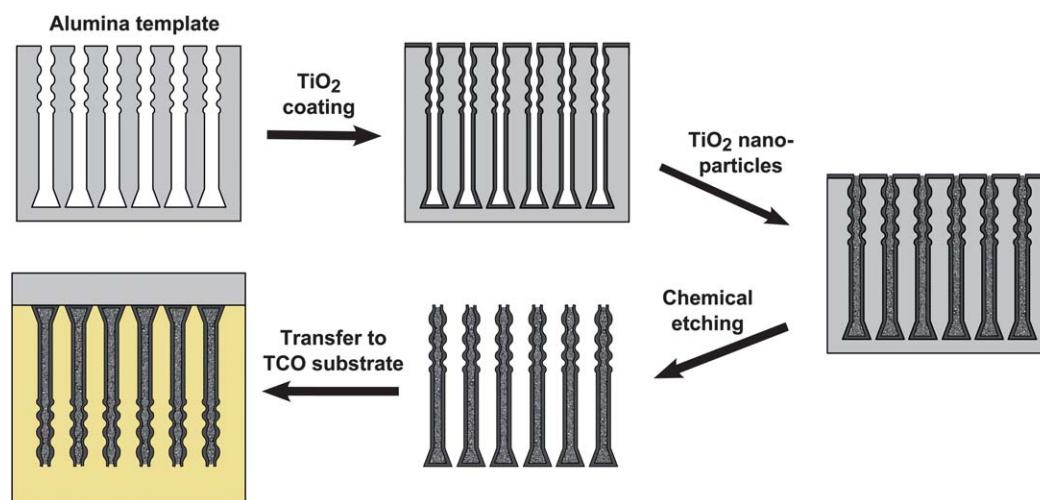


**Fig. 14** The multi-step procedure proposed for manufacturing our nanotube array: (1) modulated diameter alumina nanopores are grown from Al foil through an anodization process; (2) a thin layer of  $\text{TiO}_2$  is deposited conformally on the walls of the nanopores using either sol–gel or atomic layer deposition techniques; (3)  $\text{TiO}_2$  nanoparticles are deposited into the coated nanopores; (4) the alumina template is removed through selective etching; and (5) the nanotube array (now filled with nanoparticles) is transferred to a TCO substrate for use in a DSSC.

deposit TiO<sub>2</sub> nanoparticles selectively in only the interior of the nanotubes. This is difficult to achieve using direct anodization.

A template method is better suited to create our nanotube array. In this method alumina pores are created through anodization of an Al foil. A conformal layer of TiO<sub>2</sub> is then deposited on the walls of the pores using either sol-gel methods<sup>54</sup> or atomic layer deposition.<sup>55</sup> Chemical etching is used to selectively remove the alumina template. This leaves an array of highly ordered TiO<sub>2</sub> nanotubes that can be transferred to a TCO substrate for use in a DSSC. Like direct anodization, template anodization allows for a wide range of nanotube geometries. Deneault *et al.* have created nanotubes using this method with heights of up to 48 μm, diameters of up to 350 nm, and tube-to-tube spacings of >400 nm.<sup>54</sup> However unlike direct anodization, the use of an alumina template allows for selective deposition of nanoparticles within the nanotubes. This can be done by adding nanoparticles to the array *after* the addition of the TiO<sub>2</sub> layer to the pores, but *before* the chemical etching of the alumina. The proposed procedure is outlined in the diagram of Fig. 14.

Another requirement of our design is the ability to modulate the nanotube diameter. For anodization-based methods this is typically done by varying the applied current or voltage during growth. Periodic modulation of diameter has been demonstrated for TiO<sub>2</sub> nanotubes<sup>24,57</sup> as well as alumina nanopores.<sup>58</sup> Modulation periods from 100 nm to >2 μm have been achieved, putting our required range of roughly 200–500 nm well within current capabilities. Modulation amplitudes are typically on the order of 20–30 nm, which is somewhat less than the 50 nm assumed in this work. However given the large performance gains associated with increasing the modulation amplitude (~0.05 mA cm<sup>-2</sup> in our work), there is a strong incentive for improvements in this regard. Linear modulation of diameter has been demonstrated for alumina nanopores,<sup>59</sup> although the depth of these pores was much less than in our design.

Finally, our design features triangular corrugation of the glass-air interface for reduced reflection losses. In three dimensions this would correspond to either pyramidal or conical nanopatterning of the glass. There has been a great deal of work on nanopatterning at interfaces for anti-reflection purposes; Raut *et al.* discuss manufacturing strategies for these nanostructures at length in their review.<sup>32</sup>

## 4 Conclusions

We have demonstrated the efficacy of light-trapping in hybrid DSSCs consisting of modulated-diameter nanoparticle-filled nanotubes. Our design improves solar absorption by 33% with enhanced anti-reflection, light confinement, and back-reflection in the cell. For a C101-based photonic crystal cell it was found that periodicities on the order of 500 nm with nanotube diameters of roughly half the period are optimal for solar absorption. Chirped sinusoidal modulation at the bottom of the nanotube array provides strong back-reflection. Solar absorption is optimized for modulation period ranges of roughly 250–450 nm. Triangular corrugation at the top of the cell is effective for anti-reflection. Our final optimized structure gives an MAPD

of 20.8 mA cm<sup>-2</sup> at normal incidence, well beyond the current record for short-circuit current density in C101-based cells. This suggests that photonic crystal light-trapping is more effective than the random light scattering approach used in the best cells today. Our structure features additional advantages over traditional DSSCs, such as a frequency-selective back-reflector and the possibility of improved charge collection coming from the ordered nanotube array. Photonic crystal designs are very versatile and can be tailored to any desired dye system to increase absorption. Our results suggest that light-trapping enhancement is most effective in dyes with relatively weak absorption overall and a long absorption tail (*e.g.*, black dye<sup>60</sup>).

Given better light collection than traditional DSSCs and the potential for improved charge collection through ordered nanotube arrays, we anticipate cells with our design with power conversion efficiencies over 13%. This would be a record for DSSCs. Future research will focus on extending the model to three dimensions. Coupling of our optical model to an electrical charge transport model would enable a complete DSSC device optimization.

## Acknowledgements

The authors would like to thank Dr Guillaume Demésy for advice concerning the use of the FEM code. This work was supported in part by the United States Department of Energy under contract DE-FG02-10ER46754, the Natural Sciences and Engineering Research Council (NSERC) and the Canadian Institute for Advanced Research. Stephen Foster is grateful to NSERC for a postgraduate scholarship.

## References

- 1 M. Grätzel and B. O'Regan, *Nature*, 1991, **353**, 737–740.
- 2 A. Yella, H.-W. Lee, H. N. Tsao, C. Yi, A. K. Chandiran, M. Nazeeruddin, E. W.-G. Diao, C.-Y. Yeh, S. M. Zakeeruddin and M. Grätzel, *Science*, 2011, **334**, 629–634.
- 3 Y. Cao, Y. Bai, Q. Yu, Y. Cheng, S. Liu, D. Shi, F. Gao and P. Wang, *J. Phys. Chem. C*, 2009, **113**, 6290–6297.
- 4 J. M. Kroon, N. J. Bakker, H. J. P. Smit, P. Liska, K. R. Thampi, P. Wang, S. M. Zakeeruddin, M. Grätzel, A. Hinsch, S. Hore, U. Würfel, R. Sastrawan, J. R. Durrant, E. Palomares, H. Pettersson, T. Gruszecki, J. Walter, K. Skupien and G. E. Tulloch, *Prog. Photovoltaics*, 2007, **15**, 1–18.
- 5 M. K. Nazeeruddin, F. De Angelis, S. Fantacci, A. Selloni, G. Viscardi, P. Liska, S. Ito, B. Takeru and M. Grätzel, *J. Am. Chem. Soc.*, 2005, **127**, 16835–16847.
- 6 C.-Y. Chen, M. Wang, J.-Y. Li, N. Pootrakulchote, L. Alibabaei, C.-h. Ngoc-le, J.-D. Decoppet, J.-H. Tsai, C. Grätzel, C.-G. Wu, S. M. Zakeeruddin and M. Grätzel, *ACS Nano*, 2009, **3**, 3103–3109.
- 7 Y. Chiba, A. Islam, R. Komiya, N. Koide and L. Han, *Appl. Phys. Lett.*, 2006, **88**, 223505.
- 8 G. Demésy and S. John, *J. Appl. Phys.*, 2012, **112**, 074326.
- 9 Q. Zhang and G. Cao, *Nano Today*, 2011, **6**, 91–109.

- 10 M. Yu, Y.-Z. Long, B. Sun and Z. Fan, *Nanoscale*, 2012, **4**, 2783–2796.
- 11 K. Zhu, N. R. Neale, A. Miedaner and A. J. Frank, *Nano Lett.*, 2007, **7**, 69–74.
- 12 F. Shao, J. Sun, L. Gao, S. Yang and J. Luo, *J. Phys. Chem. C*, 2011, **115**, 1819–1823.
- 13 C.-C. Chen, H.-W. Chung, C.-H. Chen, H.-P. Lu, C.-M. Lan, S.-F. Chen, L. Luo, C.-S. Hung and E. W.-G. Diau, *J. Phys. Chem. C*, 2008, **112**, 19151–19157.
- 14 K. Shankar, G. K. Mor, H. E. Prakasam, S. Yoriya, M. Paulose, O. K. Varghese and C. A. Grimes, *Nanotechnology*, 2007, **18**, 065707.
- 15 L.-L. Li, C.-Y. Tsai, H.-P. Wu, C.-C. Chen and E. W.-G. Diau, *J. Mater. Chem.*, 2010, **20**, 2753–2758.
- 16 J. H. Park, T.-W. Lee and M. G. Kang, *Chem. Commun.*, 2008, 2867–2869.
- 17 X. Gan, X. Li, X. Gao, F. Zhuge and W. Yu, *Thin Solid Films*, 2010, **518**, 4809–4812.
- 18 C.-H. Ku and J.-J. Wu, *Nanotechnology*, 2007, **18**, 505706.
- 19 A. Hu, L. Xiao, G. Dai and Z. Xia, *J. Solid State Chem.*, 2012, **190**, 130–134.
- 20 X. Pan, C. Chen, K. Zhu and Z. Fan, *Nanotechnology*, 2011, **22**, 235402.
- 21 S. Wang, J. Zhang, S. Chen, H. Yang, Y. Lin, X. Xiao, X. Zhou and X. Li, *Electrochim. Acta*, 2011, **56**, 6184–6188.
- 22 Y. Alivov and Z. Y. Fan, *Appl. Phys. Lett.*, 2009, **95**, 063504.
- 23 Q. Zheng, H. Kang, J. Yun, J. Lee, J. H. Park and S. Baik, *ACS Nano*, 2011, **5**, 5088–5093.
- 24 C. T. Yip, H. Huang, L. Zhou, K. Xie, Y. Wang, T. Feng, J. Li and W. Y. Tam, *Adv. Mater.*, 2011, **23**, 5624–5628.
- 25 A. Chutinan and S. John, *Phys. Rev. A*, 2008, **78**, 023825.
- 26 S. Colodrero, M. Ocana and H. Míguez, *Langmuir*, 2008, **24**, 4430–4434.
- 27 S. Nishimura, N. Abrams, B. A. Lewis, L. I. Halaoui, T. E. Mallouk, K. D. Benkstein, J. van de Lagemaat and A. J. Frank, *J. Am. Chem. Soc.*, 2003, **125**, 6306–6310.
- 28 C.-a. Tao, W. Zhu, Q. An and G. Li, *J. Phys. Chem. C*, 2010, **114**, 10641–10647.
- 29 A. Mihi, C. Zhang and P. V. Braun, *Angew. Chem., Int. Ed.*, 2011, **50**, 5712–5715.
- 30 S.-L. Chen, A.-J. Wang, C.-T. Hu, C. Dai and J. B. Benziger, *AIChE J.*, 2012, **58**, 568–572.
- 31 A. Mihi and H. Míguez, *J. Phys. Chem. B*, 2005, **109**, 15968–15976.
- 32 H. K. Raut, V. A. Ganesh, A. S. Nair and S. Ramakrishna, *Energy Environ. Sci.*, 2011, **4**, 3779–3804.
- 33 S. Ito, T. N. Murakami, P. Comte, P. Liska, C. Grätzel, M. K. Nazeeruddin and M. Grätzel, *Thin Solid Films*, 2008, **516**, 4613–4619.
- 34 Z.-S. Wang, H. Kawauchi, T. Kashima and H. Arakawa, *Coord. Chem. Rev.*, 2004, **248**, 1381–1389.
- 35 H.-J. Ahn, S.-I. Kim, J.-C. Yoon, J.-S. Lee and J.-H. Jang, *Nanoscale*, 2012, **4**, 4464–4469.
- 36 H. Li, B. Jiang, R. Schaller, J. Wu and J. Jiao, *J. Phys. Chem. C*, 2010, **114**, 11375–11380.
- 37 L. M. Peter, *J. Phys. Chem. C*, 2007, **111**, 6601–6612.
- 38 J. Halme, G. Boschloo, A. Hagfeldt and P. Lund, *J. Phys. Chem. C*, 2008, **112**, 5623–5637.
- 39 S. Wenger, M. Schmid, G. Rothenberger, A. Gentsch, M. Grätzel and J. O. Schumacher, *J. Phys. Chem. C*, 2011, **115**, 10218–10229.
- 40 Y. Lin, Y. T. Ma, L. Yang, X. R. Xiao, X. W. Zhou and X. P. Li, *J. Electroanal. Chem.*, 2006, **588**, 51–58.
- 41 X. Bi-Tao, Z. Bao-Xue, B. Jing, Z. Qing, L. Yan-Biao, C. Wei-Min and C. Jun, *Chin. Phys. B*, 2008, **17**, 3713.
- 42 K. G. Ong, O. K. Varghese, G. K. Mor, K. Shankar and C. A. Grimes, *Sol. Energy Mater. Sol. Cells*, 2007, **91**, 250–257.
- 43 G. Demésey, F. Zolla, A. Nicolet, M. Commandré and C. Fossati, *Opt. Express*, 2007, **15**, 18089–18102.
- 44 M. M. ur Rahman, G. Yu, K. M. Krishna, T. Soga, J. Watanabe, T. Jimbo and M. Umeno, *Appl. Opt.*, 1998, **37**, 691–697.
- 45 S. M. Zakeeruddin, M. K. Nazeeruddin, R. Humphry-Baker, P. Pechy, P. Quagliotto, C. Barolo, G. Viscardi and M. Grätzel, *Langmuir*, 2002, **18**, 952–954.
- 46 F. Gao, Y. Wang, D. Shi, J. Zhang, M. Wang, X. Jing, R. Humphry-Baker, P. Wang, S. M. Zakeeruddin and M. Grätzel, *J. Am. Chem. Soc.*, 2008, **130**, 10720–10728.
- 47 O. Deparis, J. P. Vigneron, O. Agustsson and D. Decroupet, *J. Appl. Phys.*, 2009, **106**, 094505.
- 48 F. E. Gálvez, E. Kempainen, H. Míguez and J. Halme, *J. Phys. Chem. C*, 2012, **116**, 11426–11433.
- 49 J. R. Jennings, A. Ghicov, L. M. Peter, P. Schmuki and A. B. Walker, *J. Am. Chem. Soc.*, 2008, **130**, 13364–13372.
- 50 J.-H. Yum, E. Baranoff, S. Wenger, M. K. Nazeeruddin and M. Grätzel, *Energy Environ. Sci.*, 2011, **4**, 842–857.
- 51 I. C. Flores, J. N. de Freitas, C. Longo, M.-A. D. Paoli, H. Winnischofer and A. F. Nogueira, *J. Photochem. Photobiol., A*, 2007, **189**, 153–160.
- 52 C. Xu and D. Gao, *J. Phys. Chem. C*, 2012, **116**, 7236–7241.
- 53 J. Qiu, F. Zhuge, K. Lou, X. Li, X. Gao, X. Gan, W. Yu, H.-K. Kim and Y.-H. Hwang, *J. Mater. Chem.*, 2011, **21**, 5062–5068.
- 54 J. R. Deneault, X. Xiao, T.-S. Kang, J. S. Wang, C. M. Wai, G. J. Brown and M. F. Durstock, *ChemPhysChem*, 2012, **13**, 256–260.
- 55 J. Lee, K. S. Hong, K. Shin and J. Y. Jho, *J. Ind. Eng. Chem.*, 2012, **18**, 19–23.
- 56 S. Yoriya and C. A. Grimes, *Langmuir*, 2010, **26**, 417–420.
- 57 Y.-L. Xie, Z.-X. Li, H. Xu, K.-F. Xie, Z.-G. Xu and H.-L. Zhang, *Electrochem. Commun.*, 2012, **17**, 34–37.
- 58 W. Lee and J.-C. Kim, *Nanotechnology*, 2010, **21**, 485304.
- 59 J. Li, C. Li, C. Chen, Q. Hao, Z. Wang, J. Zhu and X. Gao, *ACS Appl. Mater. Interfaces*, 2012, **4**, 5678–5683.
- 60 M. K. Nazeeruddin, P. Pechy and M. Grätzel, *Chem. Commun.*, 1997, 1705–1706.